RSC Advances

ROYAL SOCIETY
OF CHEMISTRY

www.rsc.org/advances

Cite this: DOI: 10.1039/c0xx00000x

www.rsc.org/xxxxxx

ARTICLE TYPE

Synthesis and characterisation of nickel oxide nanofibre webs with alcohol sensing characteristics

Gibin George and S. Anandhan*

Received (in XXX, XXX) Xth XXXXXXXXX 20XX, Accepted Xth XXXXXXXXX 20XX
DOI: 10.1039/b000000x

In this study, nickel oxide (NiO) nanofibres were obtained by sol-gel electrospinning process followed by calcination from an aqueous sol of poly(2-ethyl-2-oxazoline)/nickel acetate tetrahydrate. Thermogravimetric analysis was used to determine the degradation temperature of the composite fibres, so as to get nickel oxide nanofibres. X-ray photoelectron spectroscopy and X-ray diffraction studies revealed the complete elimination of the organic phase from NiO fibres during calcination. The change in grain size with calcination temperature was determined by X-ray diffraction. The defects in fibres resulted in the modification of Raman spectra as compared with that of a single crystal. The magnetic properties of the fibres were reduced as the calcination temperature was increased; it is owing to the presence of non-stoichiometric defects. As the calcination temperature was increased, the amount of defects was reduced, which induced a difference in the band gap energy of the fibres. Sensitivity of the NiO fibres towards five different alcohols was studied, and the sensitivity towards ethanol was the highest.

Introduction

Fabrication of nanomaterials is challenging and always involves time consumption and high cost during their processing. Ceramic oxide nanomaterials are of special interest, because of their stability, semiconducting nature and low cost. Combining two or three processes together can improve the flexibility and reduce the production cost in many occurrences. For example, the technique used for the production of oxide nanomaterials by combining electrospinning, a process meant for producing polymer nanofibres, and sol-gel process, a technique used for producing ceramic materials, is efficient and cost-effective and it has several advantages of electrospinnng and sol-gel technique.

There are three steps in sol-gel electrospinning process. The sol-gel electrospinning starts with the preparation of a spinnable sol of an appropriate polymer-solvent system and a suitably selected metal salt of the desired metal oxide. Pechini's method is also an alternative for the production of sol.[1] While preparing the sol, one has to consider its viscosity, which determines the suitability of a sol for electrospinning. In the second step, sol is electrospun to form the polymer/metal salt composite nanofibres. During this process, the solvent used in forming the sol is completely eliminated and the thus obtained fibres are called, in terms of the sol-gel technique, as xerogel fibres. In the third step, the xerogel fibres are calcined above the degradation temperature of the organic part in the composite fibres to get pure oxide nanofibres.

Oxide nanomaterials are continuously gaining interest in the field of catalysis,[2,3] battery electrodes,[4-6] dye sensitive solar cells,[7-10] hydrogen evolution,[11] fuel cells,[12-14] sensors,[15-19] field emission transistors,[20-21] magnetic materials,[22-24] bone regeneration[25] etc. Oxide materials in nanoscale are stable and the structural and non-stoichiometric defects that originate from their size reduction are unique. This in turn will help them to exhibit exclusive features, which are favourable in the aforementioned applications. The aspect ratio of the oxide nanomaterials is important to overcome the drawback of their semiconducting nature and contact resistance (when zero dimensional structures are used), for those applications where electron transport is involved. A continuous electron path can be offered by nanofibres, and electrospinning is the only technique for the production of high aspect ratio nanofibres.

Many metal oxides are excellent sensor materials either in their pristine form or composite or complex forms. Semiconducting oxides are potential sensor materials because of their low cost, high sensitivity, fast response/recovery time, simple electronic interface, ease of use, low maintenance and ability to detect a large number of gases.[26] As functional materials in sensors, metal oxide sensors exhibit two functions; they are the receptors of the target analytes and at the same time they transduce these molecular information to a measurable signal.[27,28] In the case of semiconducting oxide sensors, the response is its change in resistance with the concentration of the target gases. n-type (ZnO,[29-31] TiO_2,[32,33] Nb_2O_5,[34] SnO_2[35] etc.) and p-type (NiO, Co_3O_4, etc) are the two types of semiconducting oxides

---

Department of Metallurgical and Materials Engineering, National Institute of Technology-Karnataka, Srinivas Nagar, Mangalore-575025, India
** Corresponding author: Ph: +91-824-2473762; Fax: +91-824-2474059, Email: anandtmg@gmail.com & anandhan@nitk.edu.in*

commonly used in solid state sensors.

Nickel oxide (NiO) is a p-type semiconductor known for metal-insulator transition. Also, it is antiferromagnetic in nature. As functional ceramics, NiO based materials are widely used in sensors,[36] electrochromic devices,[37] solar-energy absorbers,[38,39] lithium-ion batteries,[40] supercapacitors,[41] heterogeneous catalysts,[42] hydrogen evolution[43] and as magnetic materials.[44,45]

In this study, nanocrystalline NiO nanofibres were fabricated by calcining electrospun poly(2-ethyl-2-oxazoline) (PEtOx)/nickel (II) acetate tetrahydrate (NATH) nanofibres. The use of PEtOx as a sacrificial base for the fabrication of ceramic oxide was explored by us in an earlier study.[46] The adhesive nature of polymer can improve the final ceramic fibre morphology; in addition, ease of fibre formation can significantly help in the yield of fibres. The morphological aspects of the fibres were explored using scanning electron microscopy (SEM) and transmission electron microscopy (TEM). The compositions of the calcined NiO fibres were determined from energy dispersive X-ray spectroscopy (EDS) and an attempt has been made to understand the effect of non-stoichiometry on the magnetic and optical properties of these fibres. The ability of the NiO nanofibres to detect reducing molecules was studied by preparing the sensor elements by direct electrospinning of the NiO fibres on a quartz substrate. Methanol, ethanol and iso-propanol were used as the representative reducing target species and the effect of their molecular weight on the sensor response of the NiO nanofibres was studied.

Experimental details

Materials

PEtOx (**Fig. 1**) with a molecular weight ($\overline{M}_w$) of 500,000 obtained from Alfa Aesar, Lancs, U.K, and NATH (assay 98%) procured from Sigma Aldrich Corporation, Bangalore, India, were used without further purification as the precursors to fabricate the NiO nanofibres. Methanol, iso-propanol, 1-propanol and 1-butanol were obtained from Nice chemicals, Cochin, India, Ethanol procured from Changshu Yangyuan Chemical co., Ltd, Jiangsu, China and silver paste purchased from Siltech corporation, bangalore, India were used for the sensor studies.

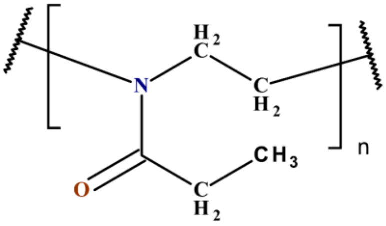

Fig. 1 Structure of poly-2-ethyl-2-oxazoline

Preparation of electrospinning solution

To prepare the spinnable sol, 2 g of PEtOx was dissolved in 10 mL of demineralized water by continuous stirring for 12 h in a closed vial. 2 g of NATH was added to the aqueous PEtOx solution and that mixture was stirred vigorously for 6 h to ensure uniform mixing of NATH in the polymer solution. The polymer to ceramic precursor ratio was maintained as 1:1 throughout this study.

Fabrication of precursor nanofibres

The PEtOx/NATH composite nanofibres were fabricated using the electrospinning technique. The precursor sol was loaded to a 10 mL syringe attached to a hypodermic needle chamfered at the tip (inner diameter: 0.5 mm and outer diameter: 0.8 mm). The syringe with the sol was loaded to a vertical electrospinning unit (E-Spin Nano, made by Physics Equipments Co., Chennai, India) and the viscous precursor solution was allowed to drip through the needle at a predetermined flow rate. When a high DC voltage was applied in between the metal spinneret (needle) and a grounded metallic collector plate covered with an aluminium foil. At a certain point, the surface tension of the sol was overcome by the electrostatic forces on the solution droplet, nanosized jets were formed from the solution at the spinneret. These nanosized jets were dried out during their travel from the spinneret to the collector plate to form nanofibres and were collected as nanofibre mat on the collector plate.

The applied voltage and flow rate during the electrospinning process were varied to optimize the fibre diameter and morphology. The concentration of the polymer solution was fixed to be 20 w/v % and the tip to collector distance was also kept constant as 25 cm. The applied voltage was varied as 15, 20 and 25 kV and the flow rates as 100, 300 and 500 µL h^{-1}. To optimize the electrospinning conditions, average fibre diameter, the diameter distribution and yield of the electrospun fibres were considered.

Preparation of ceramic nanofibres

To obtain NiO nanofibres from the electrospun precursor fibres, the precursor fibre mats, peeled off the aluminum foils were calcined in a programmable high temperature furnace (Indfur, Chennai, India) with a controllable heating rate in air. A heating rate of 4 $K.min^{-1}$ was used, followed by a dwell period of 2 h. The minimum calcination temperature was determined as 673 K, from thermogravimetric analysis (TGA) of the composite fibres. The calcination of the composite samples was performed at 673, 773 and 873 K with the same heating rate and dwell period as mentioned above.

Characterization of nanofibres

Thermogravimetric analysis (TGA) (EXSTAR 6000 TG/DTA 6300, Japan) of the composite fibres were performed in a nitrogen environment at a heating rate of 10 K min^{-1}. The morphology of the electrospun fibres before and after calcination was examined using SEM (JEOL JSM-6380LA, Japan). The samples were pasted directly on the sample holder using a carbon tape and prior to the imaging, the specimens were gold sputtered (JFC 1600 autofine coater, JEOL, Japan). The TEM (Hitachi S-5500) images of the fibres were obtained at an accelerating voltage of 30 kV. Sample for TEM analysis was prepared by placing 10 µL drop of nanofiber dispersion in acetone on a 300 mesh Cu TEM grid (Electron Microscopy Sciences) and dried completely before imaging. The compositions of the nanofibres was studied using EDS (Link ISIS-300 Micro-analytical System, Oxford Instruments, UK) attached with the SEM. An image processing software, ImageJ,[47] was used for finding the average fibre diameter from the SEM micrographs. The finer morphology of the fibres was obtained from their transmission electron micrographs (S-5500, Hitachi, Japan). FTIR spectra (Jasco FTIR 4200, Japan), in transmission mode by KBr pellet method, was recorded in a wave number range of 400 - 4000 cm^{-1} for PEtOx, PEtOx/NATH composite and NiO nanofibres for an average of 32 scans. The X-ray diffractograms (XRD) (JEOL X-ray diffractometer, DX-GE-2P, Japan) were obtained for samples calcined at three different temperatures, using CuK$_\alpha$ radiation within a range of 20-90º, at a scanning rate of 0.5 º min^{-1}. X-ray photoelectron spectra (XPS) were recorded at 25 ºC, using monochromated Al K$_\alpha$ radiation (15 keV) for excitation (Axis 165, X-ray Photoelectron Spectrometer, Kratos Analytical, UK) and a spherical mirror analyzer. The analyzed area of the sample by XPS was approximately 300 µm in diameter. UV-Vis-NIR spectra (Varian, Cary 5000 UV-Vis-NIR, USA) of the ceramic fibres were recorded in the diffused reflectance mode in the wavelength range of 215-2400 nm. Micro Raman spectra (inVia, Renishaw, UK) were collected for the nickel oxide samples prepared at different calcination temperatures, in the wave number range of 60-2000 cm^{-1} using an Argon ion laser source with a power of 100 mW and a wavelength of 514 nm. The magnetization–demagnetization curves of NiO nanofibres were recorded at 25 °C using a vibrating sample magnetometer (7404, Lake Shore Cryotronics, Inc., USA).

Sensitivity of NiO fibres

The sensitivity of NiO nanofibres for the detection of ethanol, methanol and isopropanol were evaluated. The sensing element consisted of a quartz substrate (10 mm×10 mm ×1 mm) on which the NiO nanofibres were aligned in parallel to each other. To fabricate aligned fibres on the quartz substrate, the substrate was pasted on the drum collector and the electrospinning of PEtOx/NATH composite nanofibres was carried out under the optimum operating conditions. Then the composite fibres were calcined at the respective calcination temperatures. The sensor was connected to silver electrodes using silver paste, which cross links at 150 °C. Then the elements were heated in a hot air oven up to 300 °C to achieve stability. The architecture of the sensor element is shown in **Fig. 2**.

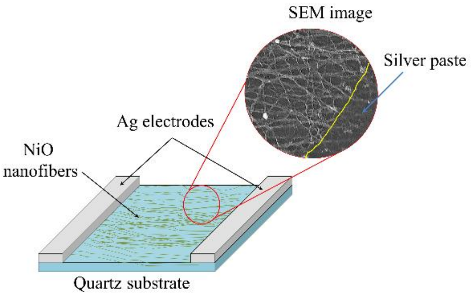

Fig. 2 The architecture of the sensor element

The sensor elements were exposed to alcohol vapours in a custom made test setup as shown in **Fig. S1** (supporting information). The vapours with known ppm were prepared by evapourating the corresponding alcohol in a chamber with a known volume. The change in resistance was measured using a multimeter (81K, MECO Meters Pvt. Ltd., Mumbai, India), as the sensor response. The sensor responses were monitored in the temperature range of 50-275 °C. The measurements were made after achieving a steady resistance at each testing temperature. The sensitivity was measured as the ratio R_g/R_a, where R_a and R_g are the resistance of the sensor in air and in the presence of target molecules, respectively.

Results and discussion

Characterization of precursor composite fibres

TGA analysis

The TGA curves of both neat PEtOx and PetOx/NATH composites are shown in **Fig. 3**. PEtOx showed a complete degradation in two steps and the complete degradation took place near 673 K, whereas, PEtOx/NATH showed many steps of degradation before it was completely turned to NiO. The first step near 373 K in both the curves is attributed to the removal of water content. The several steps in the degradation of PEtOx/NATH recognized the complex degradation in PEtOx/NATH composite, where the degradation of PEtOx and NATH occur simultaneously. The degradation products of NATH, especially the acetic acid released at the early stages, greatly influences the degradation of PEtOx and it resulted in the accelerated degradation of composite as compared with that of pristine PEtOx. The second step in the degradation profile of PEtOx/NATH composite near 600 K is due to the catalytic action of acetic acid on degrading the polymer as in **Eqn. 1**. The third and fourth steps are attributed to the conversion reactions depicted in **Eqns. 2 & 3**.[48]

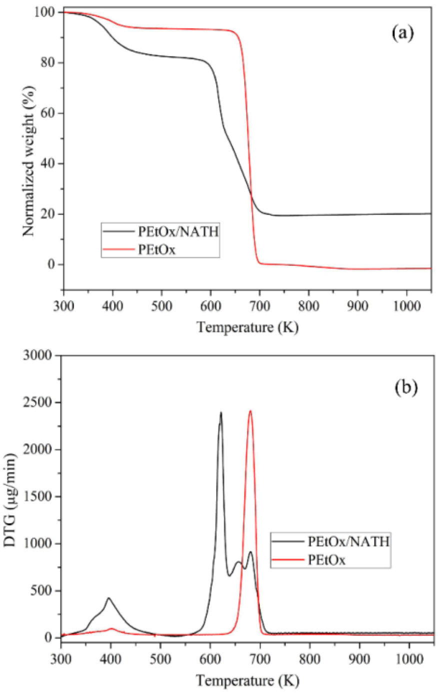

Fig. 3 (a) TG and (b) DTG plots of SAN and SAN/CATH composite fibres

$$\mathrm{Ni(CH_3COO)_2.4H_2O_{(s)} \rightarrow 0.86Ni(CH_3COO)_2.0.14Ni(OH)_{2(s)} + 0.28CH_3COOH_{(g)} + 3.72H_2O_{(g)}} \quad (1)$$

$$\mathrm{Ni(CH_3COO)_2(OH)_{2(s)} \rightarrow NiCO_{3(s)} + CH_3COCH_{3(g)} + H_2O_{(g)}} \quad (2)$$

$$\mathrm{NiCO_{3(s)} \rightarrow NiO_{(s)} + CO_{2(g)}} \quad (3)$$

SEM results

The SEM micrographs of the PEtOx/NATH composite nanofibres obtained at different applied voltages and flow rates are shown in **Fig. S2** (supporting information). At all the applied voltages and flow rates, the fibres were continuous, uniformly distributed and randomly spun on the aluminium foil, because, the concentration used here was above the critical entanglement concentration of the aqueous PEtOx solution.[46] The fibre uniformity was quantified by standard deviation (SD) and fibre uniformity coefficient (C_{FU}). The values of SD, C_{FU} and histogram of fibre diameters obtained at different applied voltages and flow rates are presented in **Fig. S2**. C_{FU} is a measure of fibre size distribution and it approaches unity when the distribution is uniform,[49]

$$C_{FU} = A_w / A_n \tag{4}$$

Where,

$$A_n = \sum n_i d_i \Big/ \sum n_i \tag{5}$$

$$A_w = \sum n_i d_i^2 \Big/ \sum n_i \, d_i \tag{6}$$

As the applied voltage was increased, regardless of the flow rate, the average fibre diameter of PEtOx/NATH composite decreased. That is because of the increase in the charge carrier concentration on the solution droplet at the needle tip.[50] When the applied voltage is increased above a certain point, i.e, above 20 kV, corona discharge was observed, therefore, no significant change in the fibre diameter was observed at those voltages,[51] therefore, 20 kV was chosen as the optimum applied voltage.

Similarly, as the flow rate was increased from 100 to 500 μL. h^{-1}, the average fibre diameter of the composites increased, because of the excess of solution available at the spinneret. The highest average fibre diameter is observed at a flow rate of 500 μL h^{-1}; therefore, this flow rate is omitted from the optimization. When the yield of the fibres is considered, at 300 μL h^{-1} it is higher than that obtained at 100 μL h^{-1}. There was no appreciable difference in the average fibre diameter when the flow rate was increased from 100 to 300 μL h^{-1}. Therefore, an applied voltage of 20 kV, a tip to collector distance of 25 cm and a flow rate of 300 μL h^{-1} were taken as the optimum electrospinning conditions for the fabrication of precursor fibres.

FTIR spectroscopy

To understand the interaction between PEtOx and NATH, the FTIR spectra of NATH, PEtOx and PEtOx/NATH composite were compared (**Fig. S3,** supporting information**)**. There are a couple of new peaks in the PEtOx/NATH composite spectrum, which are considered as the interactive peaks of PEtOx and NATH. These peaks are at 1486 and 1287 cm^{-1}, which are attributed to the C-O stretching and COO stretching, respectively. The increased intensity of theses peaks in PEtOx/NATH composite and the appearance of new peaks give an indication of a good interaction between PEtOx and NATH.

Characterization of the nickel oxide nanofibre mats

The complete elimination of the organic part from the fibre was confirmed by TGA analysis of the NiO fibres calcined at lowest calcination temperature i.e., 673 K. There was no significant weight loss from NiO fibre till a temperature of 1273 K (**Fig. S4**, supporting information) other than moisture at 373 K.

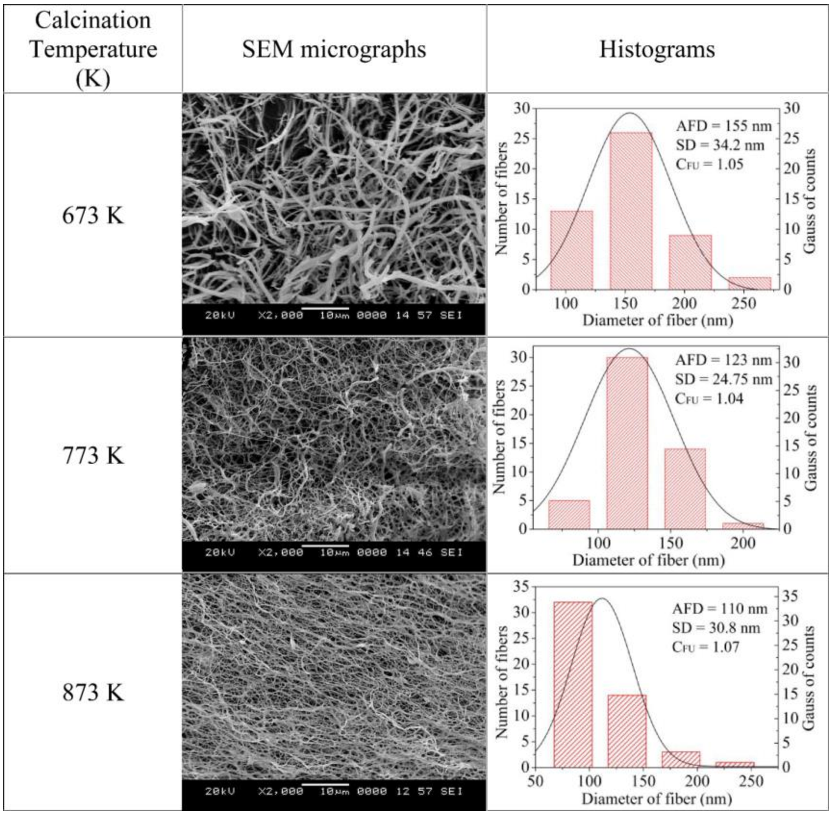

Fig. 4 SEM micrographs and histograms (50 fibres) of electrospun PEtOx/NATH fibres at different applied voltages (15, 20 and 25 kV) and flow rates (100, 300 and 500 μL.h^{-1}). The insets in histogram represent average fibre diameter (AFD), fibre uniformity coefficient (CFU) and standard deviation in fibre diameter (SD).

SEM results of NiO naofibres

The SEM micrographs of NiO nanofibres obtained at different calcination temperatures and the respective histograms are shown in **Fig. 4**. The fibre diameter was reduced as the calcination temperature was increased; it is due to the densification of grains in the fibres with an increase in calcination temperature. The NiO nanofibres have a lower AFD than the precursor composite fibres due to the complete degradation of the organic phase and the resultant shrinkage. Nanofibres of AFD lower than 100 nm were obtained at a calcination temperature of 873 K.

TEM results

The TEM micrograph of the NiO nanofibre obtained at a calcination temperature of 873 K is shown in **Fig. 5.** The serrated edges of the fibre in **Fig. 5a** reveal the numerous nanosized grains that constitute the fibre. The selected area electron diffraction (SAED) pattern (**Fig. 5b**) is indexed to the planes of diffraction that correspond to NiO. The polycrystalline nature of the fibre is revealed from **Fig. 5c**, where different planes of orientation in neighbouring grains are seen. **Fig. 5d** shows the lattice fringes corresponding to the (111) plane of NiO.

XRD results

XRD patterns of the NiO nanofibres obtained at different calcination temperatures are shown in **Fig. 6**. The sharp well defined peaks in the diffraction pattern correspond to crystalline NiO, and these patterns were compared with the standard JCPDS-01-1239 line diffraction pattern of NiO. The intensity of the diffraction patterns were increasing as the calcination temperatures were increased. It is due to the grain size enlargement and densification of the fibres as the calcination temperature is increased. No evidence of secondary oxides such as, Ni_2O_2, Ni_2O_3 etc. were found from the XRD analysis, since there were no characteristic peaks with the respective standard JCPDS line diffraction patterns.

The approximate crystallite size or grain size (*D*) of the oxide fibres is obtained by the modified Scherrer relation introduced by Williamson and Hall[52] (see supporting information) The increase in the grain size with the calcination temperature is not linear.[53] The difference in the grain size is reduced as the calcination temperatures are increased to 773 and 873 K, because the diffusion of atoms/ions across grain boundary with temperature has size dependence. As the size of the grain increases and the sizes of the grains are above a certain critical size, the surface energy of grains is decreased and the chance of diffusion will be negligible.

Similar to Oswald ripening in solutions, the bigger grains in the nanofibres are grown at the expense of smaller ones. In general, atoms/ions move from the surface with a small curvature to a surface with large curvature across the grain boundary. The atoms at the surface with low curvature have high surface energy, as in the case of small grains. The influence of temperature on grain size can be corroborated by Arrhenius equation (see supporting information): The obtained and calculated grain sizes of the fibres are presented in **Table 1**.

Table 1 Crystalline parameters of NiO nanofibres calcined at 673, 773, and 873 K

Calcination temperature (K)	Crystallite size (D) (nm)	Lattice Strain (%)	Grain size from Arrhenius equation (nm)
673 K	19.30	0.00001	19.3
773 K	28.32	0.003	24.85
873 K	44.76	0.0034	30.20

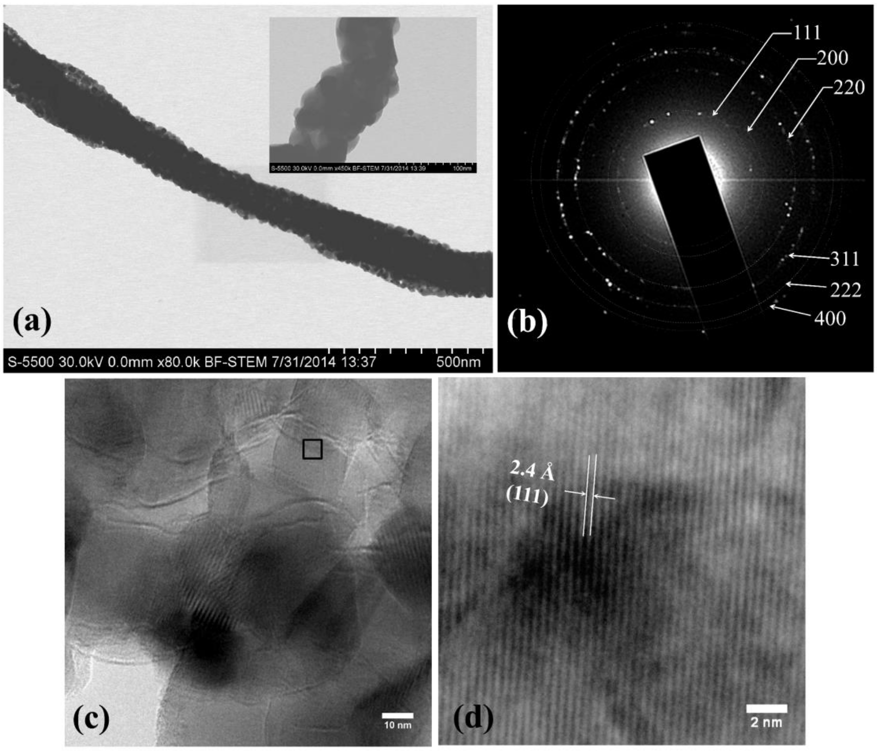

Fig. 5 TEM images of NiO nanofibre calcined at 873 K (a) TEM image of the fibre with serrated edges, inset shows a magnified image (b) SAED pattern of NiO nanofibre. (c) high magnification image with grains oriented in different directions (d) the lattice fringes of NiO corresponding to (111) plane.

Table 2 EDS results of nickel oxide obtained at various calcination temperatures

Element	Mass percentage (%)				Atomic percentage (%)			
	673 K	773 K	873 K	theoretical	673 K	773 K	873 K	theoretical
Nickel	71.69	76.64	78.51	78.58	40.83	47.19	49.89	50
Oxygen	28.31	23.36	21.49	21.42	59.17	52.81	50.11	50

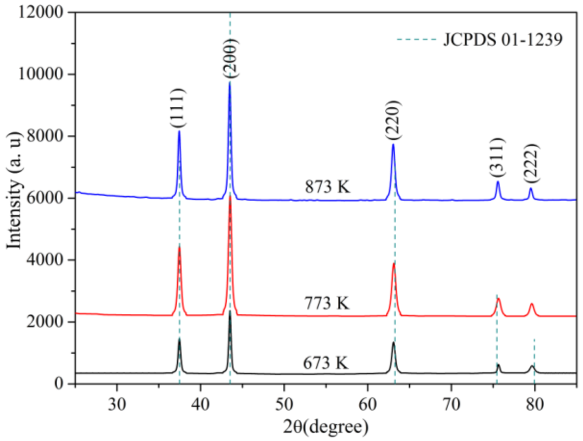

Fig. 6 X-ray diffraction patterns of NiO nanofibres calcined at 673, 773 and 873 K along with JCPDS 01-1239 line plot of NiO. The planes corresponding to each peak are shown in brackets.

EDS results

Table 2 compares the theoretical mass and atomic percentage of NiO with the SEM-EDS results of NiO nanofibres obtained at different calcination temperatures. The atomic and mass percentages of nickel and oxygen are approaching their theoretical values as the calcination temperature is increased. The rate of oxygen adsorption on a p-type material is higher than that of an n-type material such as TiO_2, due to the presence of holes in p-type oxides. As the calcination commences, this adsorbed oxygen, will occupy the lattice sites and thus increases the oxygen content in fibres. As the calcination temperature increases the stability of these oxygen molecules may decrease and they will be detached from the surface thereby maintaining a stoichiometry close to that of a perfect crystal at high calcination temperatures.

XPS results

The XPS spectral peaks of Ni 2p were deconvoluted by Gaussian curves and the spectrum comprised of two regions representing the Ni 2p3/2 (850-865 eV) and Ni 2p1/2 (870-885 eV) spin-orbit levels. This double peak of Ni (2p), corresponds to the Ni (2p3/2) and Ni (2p1/2) located at a binding energy of 854.88 and 872.1 eV, respectively as in **Fig. 7**. The shake-up satellite peaks were observed at ~6.4 eV and ~7.13 eV higher binding energy than that of Ni (2p3/2) and Ni (2p1/2) peaks, respectively. The peak of Ni (2p3/2) at a binding energy of 854.88 with their concomitant shake-up satellite peaks at 861.28 indicated the presence of Ni^{2+} cations and not of Ni^{3+} cations and the same is observed for Ni (2p1/2) peak also. This observation confirmed the NiO fibre composed of pure NiO phase.[54, 55] Especially, the absence of multiplet splitting of the peaks at 854.88 eV, which corresponds to the oxidation state of Ni^{2+}confirms the formation of NiO alone rather than any other oxidation states of nickel. The observed energy separation between Ni (2p3/2) and Ni (2p1/2) peaks are 17.22 eV, which also supports the existence of NiO alone rather than any other oxide of nickel phase as per earlier reports.[56]

The spectra of O1s and C1s (**Fig. S6&S7**, supporting information) also support the nature of peaks observed in Ni2p spectrum. In O1s spectrum, the peak at 529.62 eV corresponds to the O-1s core level of the O^{2-} anions in the NiO. The peak at 531.39 eV can be attributed to oxygen in the defect sites within the oxide crystal [55] or adsorbed oxygen[55, 56] or hydroxide species.[56] In the C-1s spectrum of carbon, the peaks represent the presence of atmospheric carbon, which is very likely and, in fact, it is often used to calibrate peak positions.

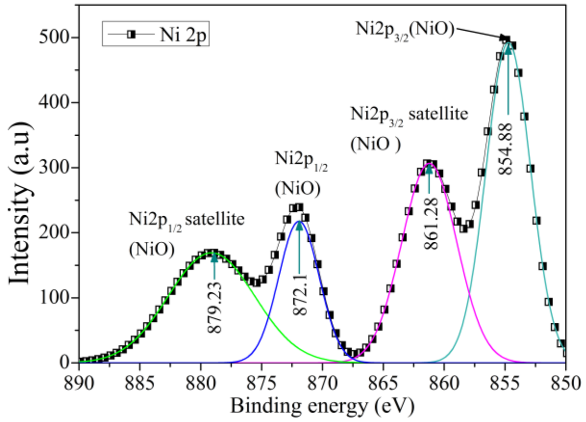

Fig. 7 Ni 2p XPS of the NiO nanofibers calcined at 673 K

FTIR, Raman and UV-Vis-NIR spectroscopy

FTIR spectra of the NiO nanofibres obtained at different calcination temperatures are shown in **Fig. 8.** The peak at 463 cm^{-1} is due to the nickel-oxygen covalent bond. The peaks corresponding to the organic part of the precursor composite fibres disappeared due to calcination. Peak intensification and broadening was observed as the calcination temperature was increased, which is due to the densification and grain size enhancement of fibres as the calcination temperature is increased.

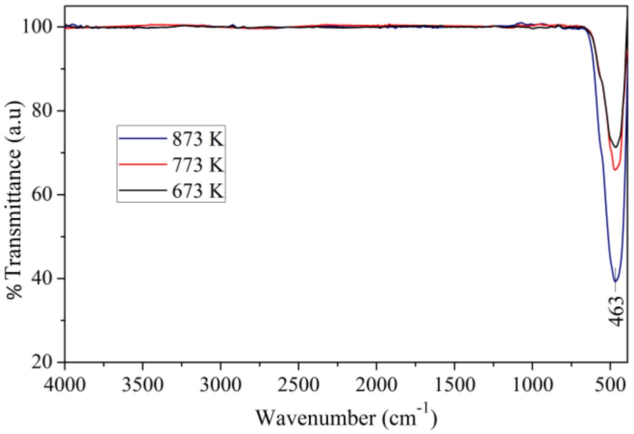

Fig. 8 FTIR spectra of NiO nanofibres obtained by calcination at 673, 773 and 873 K.

Raman spectra of the NiO nanofibres calcined at different temperatures are shown in **Fig. 9**. The peaks below 600 cm^{-1} are due to first order scattering, and the ones above 600 cm^{-1} are due to second order scattering. The forbidden phonon scattering is also present in NiO nanofibres and those peaks are assigned to 1-phonon scattering (83.6 and 198.1 cm^{-1}), which are absent in NiO single crystal.[57] These phonon scattering are due to the presence of lattice defects, that lower the symmetry around the atoms normally participating in the formation of phonons in a perfect single crystal; and the non-stoichiometry in the composition of oxygen is considered to be the major reason behind this phenomena.[58] NiO is an antiferromagnetic material; it has two types of magnons associated with the spin of electrons in two types of atoms; one with spins up and the other with spins down. The nature of magnons depends on the structure of NiO at ground state.[59] The disappearance of 2-magnon peak (1401 cm^{-1}) is attributed to the complete transition from antiferromagnetic to ferromagnetic nature of NiO nanofibres obtained at 673 K. The intensity of the peaks is increasing with the calcination temperature, which may be attributed to the grain growth and densification of fibres with calcination temperature. The intense peak at 506 cm^{-1} has originated from the defects, which is absent in the case of a perfect NiO crystal.[57]

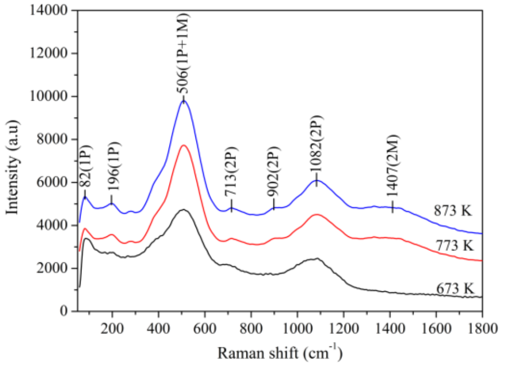

Fig. 9 Raman spectra of NiO fibres calcined at 673, 773 and 873 K.

UV-Vis-NIR spectra of NiO nanofibres obtained at different calcination temperatures are shown in **Fig. 10.** The absorbance peaks of NiO as in **Fig. 10** are due to the internal transitions of Ni^{2+}. The singlet transition ($^3T_{1g}(P) \rightarrow ^3A_{2g}(F) \sim 24000\,cm^{-1}$) is stronger than the triplet-triplet transition of Ni^{2+} at 14900 cm^{-1} ($^3T_{1g}(F) \rightarrow ^3A_{2g}(F)$) and 8700 cm^{-1} ($^3T_{2g}(F) \rightarrow ^3A_{2g}(F)$) in NiO single crystals. The peak at 8700 cm^{-1} has disappeared in the synthesized NiO nanofibres because of the non-stoichiometry of nickel and oxygen.[60] A slight shift in the transition peaks was observed as the calcination temperatures was increased, which is due to the improvement in the stoichiometry at high calcination temperatures, as observed in EDS results.

The optical band gap energy and Urbach energy of the fibres obtained at different calcination temperatures were estimated (**Fig. S8**, supporting information) and are presented in **Table 3**. The band gap energy is increasing as the calcination temperatures are increased. The change in band gap energy with calcination temperatures is attributed to the non-stoichiometry in the composition of nickel and oxygen in the obtained fibres. The difference in stoichiometry was revealed by the EDS results and this factor is anticipated to affect the magnetic properties of the NiO nanofibres. The difference in band gap energy is due to the modification of the band gap in the presence of defects, which is termed as the Urbach energy;[61, 62] and Urbach energy is an indirect way of specifying the amount of defects present in an oxide system. From the Urbach energy calculation, it is concluded that the maximum amount of stoichiometric defects are observed in the fibres calcined at 673 K.

Table 3 Band gap energy and Urbach energy of the NiO nanofibres calcined at 673, 773, and 873 K.

Calcination Temperature (K)	Band gap (eV)	Urbach Energy (eV)
673	3.12	0.36
773	3.14	0.35
873	3.16	0.33

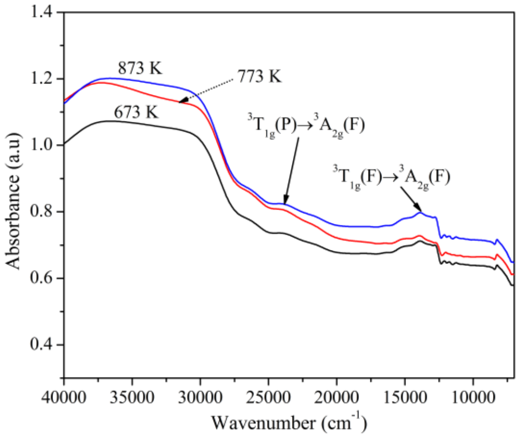

Fig. 10 UV-Vis-NIR spectra of NiO fibres calcined at 673, 773 and 873 K

Magnetic properties

The magnetic properties, at room temperature (**Table 4**), of the fibres obtained at different calcination temperatures were obtained by the magnetization-demagnetization curves, which are shown in **Fig. 11.** The fibres are of nanoscale in diameter and the majority of the atoms composing the fibres are on their surfaces; therefore, the electronic and magnetic properties of the fibres are determined by the properties of the atoms on their surfaces. The size of the hysteresis loops were waning as the calcination temperatures were increased. The reduction in the magnetic properties of the fibres with increasing calcination temperature can happen because of two reasons. The first is due to the non-stoichiometry of the elements in the fibre and the second is due to the growth of the grains. As the calcination temperature is increased the stoichiometric ratio approaches the theoretical values as observed in EDS analysis (**Table 2**). Under oxygen rich condition, the dominant defect in NiO is Ni vacancies and it can influence the magnetic properties of NiO based on the ionization state of the vacancy.[63] The decrease in magnetic properties with grain size can be attributed to the splitting of magnetic domain in the crystals with sizes above the critical single domain size.[64] The 2-magnon peak in the Raman spectrum of the NiO fibres obtained at 673 K, which corresponds to the antiferromagnetic properties of NiO, is diminished as compared with that of fibres obtained at the higher temperature.

Table 4 Saturation magnetization of NiO nanofibres at 25 °C.

Calcination temperature (K)	Remanence (emu/g)	Coercivity (G)
673	15.15×10^{-4}	136.21
773	4.54×10^{-4}	89.3
873	2.83×10^{-4}	80.27

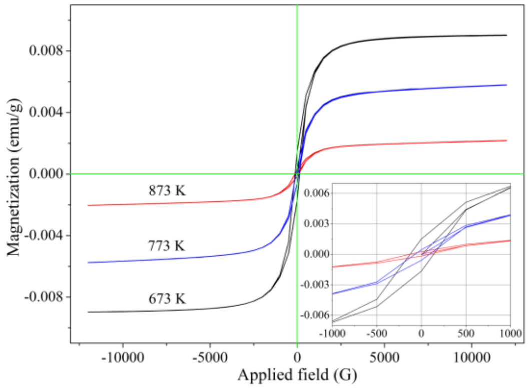

Fig. 11 Magnetization-demagnetization curves at 25 °C of the NiO nanofibres calcined at 673, 773 and 873 K.

Sensitivity of NiO fibres towards alcohols

The critical sensing temperature of NiO nanofibres was obtained from the sensor response-temperature plot of NiO fibres obtained at 673 K shown in **Fig. 12**, the concentration of target vapours were 100 ppm. The change in resistance of the fibres in the presence of the alcohols was considered as the sensory response. The sensory response of the fibres toward alcohols is a function of temperature; and the sensitivity was increasing as the temperature was increased and reaches maximum at a certain critical value. This critical temperature was changed as the target vapours were changed, since the reducing abilities of the molecules used in the present study are different. The maximum sensing temperature for each target molecule is shown by an arrow in **Fig. 12.**

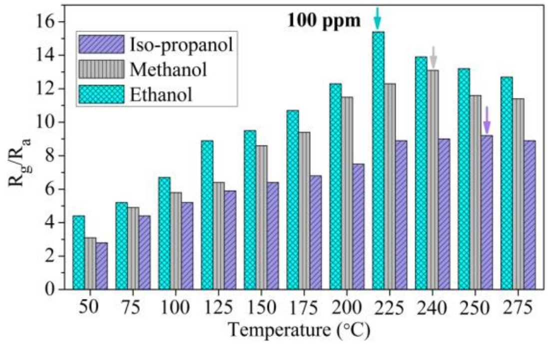

Fig. 12 The sensor response-temperature plot of NiO nanofibres obtained at 673 K

The gas-sensing mechanism is based on the changes in the conductance of the sensing layers of the semiconductor catalytic material NiO. The conductance of the oxide-based sensor is mainly influenced by the oxygen adsorbed on the surface of the materials, and the affinity of oxygen towards p-type materials is more than that of an n-type material. The sensitivity is determined by the chemical reaction of this adsorbed oxygen with the target vapour/gas, which can be either oxidation or reduction. Therefore, the efficiency of vapour/gas sensing mainly depends on the surface properties of the catalytic oxide material, nature of the gas to be detected and the operating temperature.[65] The operating temperature also has a great influence on the sensitivity towards gas. With increasing temperature in air, oxygen will be adsorbed on the surface of the catalytic sensing material, which subsequently undergoes the following reactions (**Fig. 13a**).

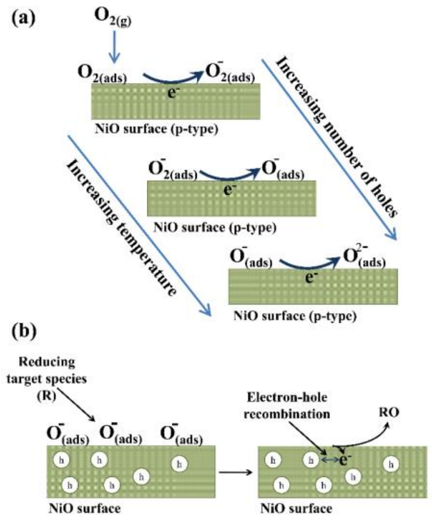

Fig. 13 (a) Interaction of the NiO nanofiber surface with oxygen at various temperatures (b) mechanism of response at critical temperature

The electrical conductivity of the p-type semiconductor materials increases (or decreases) with the adsorption of oxidizing (or reducing) gases on their surfaces and is just opposite in the case of n-type materials.[66] The oxygen species capture electrons from the conduction band of the p-type semiconductor sensing material, that is NiO, leading to the increased hole concentration. These holes can improve the conductivity of the material in p-type semiconductors. Then the reducing gas can react with the oxygen adsorbed on the surface of the sensor and a typical interaction is explained in **Fig. 13b.**[66,67]

During the oxidation of alcohol by the adsorbed oxygen on the catalytic surface, electrons are generated. These electrons are combined with the holes in the fibres, as a result, the hole concentration decreases, which results an increase in the resistance. Since holes are the major charge carriers in p-type semiconductors, the decrease in number of holes will result in the decrease of conductivity, in other words, an increase in resistance. This change in the electrical conductivity is nothing but the sensitivity of the NiO based sensor to alcohols. The surface is completely saturated with adsorbed oxygen gas at any sensing temperature; hence, the possibility of reaction between the reducing gas and lattice oxygen is neglected.

The effect on sensitivity with increasing vapour concentrations was studied by monitoring the changes in resistance of the NiO nanofibres at critical temperature. The response from the sensor based on the fibres obtained at 673 K is the highest and the difference is appreciable at a high concentration of the targeted species. In the present study, the amount of adsorbed oxygen is the highest in the NiO fibres calcined at 673 K (**Fig. 14**). The NiO nanofibres obtained at 673 K are composed of smaller grains as measured from the XRD results. The good sensing efficiency of materials with a small grain size and a large specific area is attributed to their increased rates of adsorption of oxygen and the gas to be detected (reducing or oxidizing gas).[68] The nanofibres obtained at 673 K are porous and as the calcination temperature is increased the porosity of NiO nanofibres decreases. As a result, the average diameter of the NiO nanofibres decreases as the calcination temperature is increased. Since the porosity of the fibres obtained at 673 K is the highest for which the grain sizes are also less, the Debye length (λ_D) – a measure of the field penetration into the bulk (electron depletion region), of these fibres are the highest.[69] As the grain size decreases, the Debye length increases and matches with the dimensions of the grains; then, the electronic properties of the materials are affected by the adsorption/desorption of molecules on the surface.

The sensitivity of NiO fibres toward ethanol vapour is more as compared with that of methanol and iso-propanol at all the temperatures (**Fig. 12**) and concentration (**Fig.15**) used. The greater sensitivity is towards ethanol vapours followed by methanol and isopropanol vapours, because, primary alcohols with a higher number of (-CH_2-) groups are more easily decomposed and oxidized or reduced.[70,71] As a result, ethanol, which has the highest number of CH_2 groups, is easily decomposed and caused the largest changes in free carrier density within the NiO nanofibres than methanol. Secondary alcohols are less prone to oxidation and decomposition as compared with primary alcohols; hence, the NiO nanofibres exhibit the lowest sensitivity to isopropanol. To confirm the dependence of sensitivity on the number of –CH_2– groups in alcohols, the sensitivity of NiO nanofibres towards 1-propanol and 1-butanol were also estimated and an aforementioned trend is observed in the sensitivity of those alcohols also (**fig. 15**).

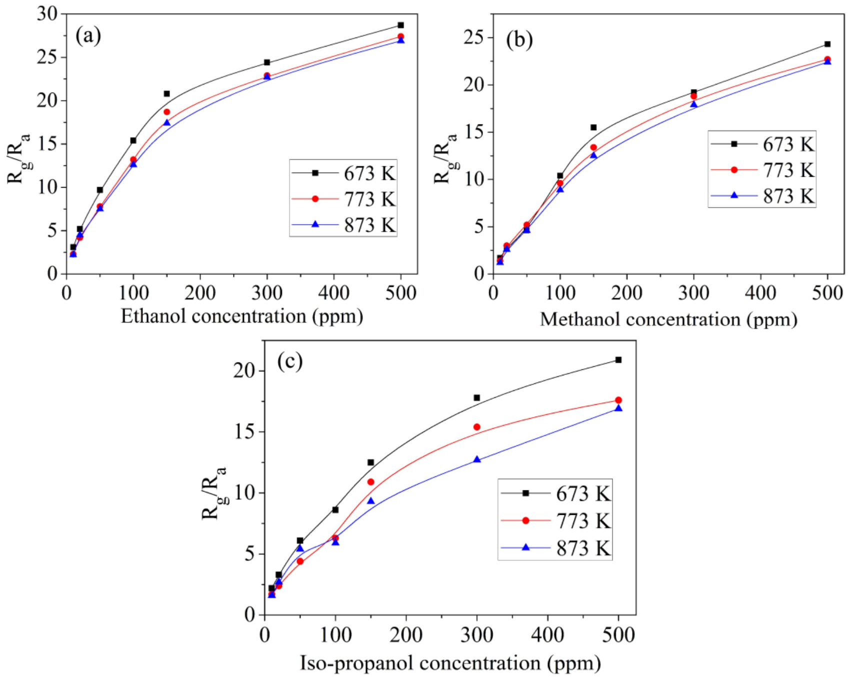

Fig. 14 The response-concentration plots of NiO nanofibres obtained at different calcination temperature for (a) ethanol at 225 °C, (b) methanol at 240 °C and (c) iso-propanol at 250 °C.

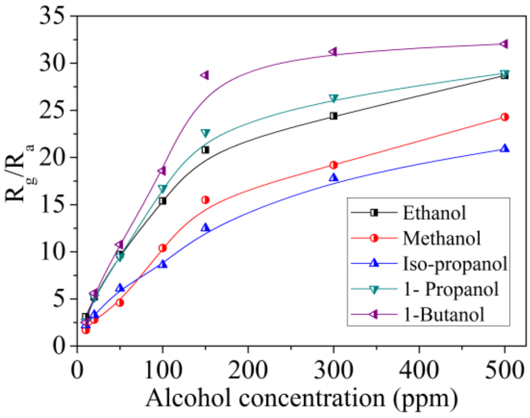

Fig. 15 A comparison on sensor response of NiO nanofibres calcined at 673 K to ethanol, methanol, 1-propanol, 1-butanol and iso-propanol vapours.

Conclusions

In summary, NiO nanofibres were successfully fabricated by sol-gel electrospinning method, using PEtOx/NATH composite precursor fibres. AFD of the precursor composite fibres decreased as the applied voltage was increased from 15 to 20 kV; but, above 20 kV the reduction in fibre diameter was not appreciable because of the corona discharge. A flow rate of 300 $\mu L.h^{-1}$ at 20 kV was the optimum electrospinning condition for the fabrication of PEtOx/NATH composite fibres. TEM images revealed that the NiO nanofibres are polycrystalline in nature. The grain sizes of the NiO nanofibres increased with an increase in the calcination temperature. The reduction in the magnetic properties of the NiO nanofibres with calcination temperature is attributed to the improvement in stoichiometry of nickel and oxygen in the fibres. The difference in oxygen content affects the band gap energy of the fibres, as observed in the UV-vis-NIR analysis. The presence of defects modified the Raman bands of the fibres as compared with that of the single NiO crystal. The NiO nanofibres exhibit good sensitivity toward ethanol, methanol and iso-propanol. The highest sensitivity was exhibited by the NiO fibres obtained at 673 K, which had smaller grains and high adsorbed oxygen as compared with those obtained at higher calcination temperatures.

Acknowledgments

Gibin George would like to thank the Department of Metallurgical and Materials Engineering, National Institute of Technology of Karnataka (NITK), India, for the research fellowship. The authors thank Ms. U. Rashmi and Ms. Akshata G. Patil for their kind assistance in scanning electron microscopy and x-ray diffraction, respectively. CIF, Pondicherry University, India, is acknowledged for its kind assistance in Raman spectra and VSM studies of the samples. The authors are very grateful to STIC, Cochin, India for the UV-Vis-NIR analysis of the samples.

References

1. S. Sakka, *Handbook of sol-gel science and technology. 1. Sol-gel processing*, Kluwer academic publishers, MA, 2005.
2. S. W. Verbruggen, M. Keulemans, M. Filippousi, D. Flahaut, G. Van Tendeloo, S. Lacombe, J. A. Martens and S. Lenaerts, *Appl. Catal., B*, 2014, **156–157**, 116–121.
3. G. Marbán, I. López, T. Valdés-Solís and A. B. Fuertes, *Int. J. Hydrogen Energy*, 2008, **33**, 6687–6695.
4. O. C. Compton, A. Abouimrane, Z. An, M. J. Palmeri, L. C. Brinson, K. Amine and S. T. Nguyen, *Small*, 2012, **8**, 1110–1116.
5. A. L. Viet, M. V. Reddy, R. Jose, B. V. R. Chowdari and S. Ramakrishna, *J. Phys. Chem. C*, 2010, **114**, 664–671.
6. S. Ke, F. Zheng-Wen, L. Hai-Wei, L. Da, Z. Wei and L. Yue-Sheng, *J. Inorg. Mater*., 2009, **24**, 357.
7. W. H. Jung, N.-S. Kwak, T. S. Hwang and K. B. Yi, *Appl. Surf. Sci*., 2012, **261**, 343–352.
8. K. Park, E. Jin, H. Gu, S. Yoon, E. Han and J. Yun, *Appl. Phys. Lett*., 2010, **97**, 023302–023302–3.
9. T. Krishnamoorthy, M. Z. Tang, A. Verma, A. S. Nair, D. Pliszka, S. G. Mhaisalkar and S. Ramakrishna, *J. Mater. Chem*., 2012, **22**, 2166–2172.
10. F. Iskandar, A. B. Suryamas, M. Kawabe, M. M. Munir, K. Okuyama, T. Tarao and T. Nishitani, *Jpn. J. Appl. Phys*., 2010, **49**, 010213.
11. M. Ni, M. K. H. Leung, D. Y. C. Leung and K. Sumathy, *Renewable Sustainable Energy Rev*., 2007, **11**, 401–425.
12. L. Mendoza, V. Albin, M. Cassir and A. Galtayries, *J. Electroanal. Chem.*, 2003, **548**, 95–107.
13. S. McIntosh and R. J. Gorte, *Chem. Rev*., 2004, **104**, 4845–4866.
14. M. Zhi, S. Lee, N. Miller, N. H. Menzler and N. Wu, *Energy Environ. Sci*., 2012, **5**, 7066–7071.
15. P. Sowti Khiabani, A. Hosseinmardi, E. Marzbanrad, S. Ghashghaie, C. Zamani, M. Keyanpour-Rad and B. Raissi, *Sens. Actuators, B*, 2012, **162**, 102–107.
16. A. Y. Lyashkov, A. S. Tonkoshkur, J. A. Aguilar-Martinez, and A. B. Glot, *Ceram. Int*., 2013, **39**, 2323–2330.
17. Q. Qi, T. Zhang, L. Liu, X. Zheng and G. Lu, *Sens. Actuators, B*, 2009, **141**, 174–178.
18. W. Wang, Z. Li, L. Liu, H. Zhang, W. Zheng, Y. Wang, H. Huang, Z. Wang and C. Wang, *Sens. Actuators, B*, 2009, **141**, 404–409.
19. S.-W. Choi, J. Zhang, K. Akash and S. S. Kim, *Sens. Actuators, B*, 2012, **169**, 54–60.
20. Z. Fan, D. Wang, P.-C. Chang, W.-Y. Tseng and J. G. Lu, *Appl. Phys. Lett*., 2004, **85**, 5923–5925.
21. B. Varghese, C. H. Teo, Y. Zhu, M. V. Reddy, B. V. R. Chowdari, A. T. S. Wee, V. B. C. Tan, C. T. Lim and C.-H. Sow, *Adv. Funct. Mater*., 2007, **17**, 1932–1939.
22. A. Baranowska-Korczyc, A. Reszka, K. Sobczak, B. Sikora, P. Dziawa, M. Aleszkiewicz, Ł. Kłopotowski, W. Paszkowicz, P. Dłużewski, B. J. Kowalski, T. A. Kowalewski, M. Sawicki, D. Elbaum and K. Fronc, *J. Sol-Gel Sci. Technol*., 2012, **61**, 494–500.
23. Y. Koseoglu, F. Kurtulus, H. Kockar, H. Guler, O. Karaagac, S. Kazan and B. Aktas, *J. Supercond. Nov. Magn*., 2012, **25**, 2783–2787.
24. Z. Wang, X. Liu, M. Lv, P. Chai, Y. Liu, X. Zhou and J. Meng, *J. Phys. Chem. C*, 2008, **112**, 15171–15175.
25. K. S. Brammer, C. J. Frandsen and S. Jin, *Trends Biotechnol*., 2012, **30**, 315–322.
26. J.-K. Choi, I.-S. Hwang, S.-J. Kim, J.-S. Park, S.-S. Park, U. Jeong, Y. C. Kang and J.-H. Lee, *Sens. Actuators, B*, 2010, **150**, 191–199.
27. N. Yamazoe, G. Sakai and K. Shimanoe, *Catal. Surv. Asia*, 2003, **7**, 63–75.
28. M. E. Franke, T. J. Koplin and U. Simon, *Small*, 2006, **2**, 36–50.
29. H.-U. Lee, K. Ahn, S.-J. Lee, J.-P. Kim, H.-G. Kim, S.-Y. Jeong and C.-R. Cho, *Appl. Phys. Lett*., 2011, **98**, 193114–193114–3.
30. Stafiniak, B. Boratyński, A. Baranowska-Korczyc, A. Szyszka, M. Ramiączek-Krasowska, J. Prażmowska, K. Fronc, D. Elbaum, R. Paszkiewicz and M. Tłaczała, *Sens. Actuators, B*, 2011, **160**, 1413–1418.
31. W.-Y. Wu, J.-M. Ting and P.-J. Huang, *Nanoscale Res. Lett.*, 2009, **4**, 513–517.
32. O. Landau and A. Rothschild, *Sens. Actuators, B*, 2012, **171–172**, 118–126.
33. X. Wang, F. Cui, J. Lin, B. Ding, J. Yu and S. S. Al-Deyab, *Sens. Actuators, B*, 2012, **171–172**, 658–665.
34. L. Chambon, A. Pauly, J. P. Germain, C. Maleysson, V. Demarne and A. Grisel, *Sens. Actuators, B*, 1997, **43**, 60–64.
35. Q. Qi, T. Zhang, L. Liu and X. Zheng, *Sens. Actuators, B*, 2009, **137**, 471–475.
36. J. A. Dirksen, K. Duval and T. A. Ring, *Sens. Actuators, B*, 2001, **80**, 106–115.
37. X. H. Xia, J. P. Tu, J. Zhang, X. L. Wang, W. K. Zhang and H. Huang, *Sol. Energy Mater. Sol. Cells*, 2008, **92**, 628–633.
38. G. Katumba, A. Forbes, L. Olumekor and G. Makiwa, in Proc. SPIE 7046, *Optical Modeling and Measurements for Solar Energy Systems II*, ed. B. K. Tsai, 2008, p. 70460B–70460B–8.
39. K. T. Roro, B. Mwakikunga, N. Tile, B. Yalisi and A. Forbes, *Int. J. Photoenergy*, 2012, DOI:10.1155/2012/678394
40. A. K. Rai, L. Tuan Anh, C.-J. Park and J. Kim, *Ceram. Int*., 2013, **39**, 6611–6618.
41. S. Vijayakumar, S. Nagamuthu and G. Muralidharan, *ACS Appl. Mater. Interfaces*, 2013, **5**, 2188–2196.
42. Y. Wang, J. Zhu, X. Yang, L. Lu and X. Wang, *Thermochim. Acta*, 2005, **437**, 106–109.
43. M. Gong, W. Zhou, M.-C. Tsai, J. Zhou, M. Guan, M.-C. Lin, B. Zhang, Y. Hu, D.-Y. Wang, J. Yang, S. J. Pennycook, B.-J. Hwang and H. Dai, *Nat. Commun*., 2014, **5**, DOI:10.1038/ncomms5695
44. S. Thota and J. Kumar, *J. Phys. Chem. Solids*, 2007, **68**, 1951–1964.
45. M. P. Proenca, C. T. Sousa, A. M. Pereira, P. B. Tavares, J. Ventura, M. Vazquez and J. P. Araujo, *Phys. Chem. Chem. Phys.*, 2011, **13**, 9561–9567.
46. G. George and S. Anandhan, *J. Sol-Gel Sci. Technol.*, 2013, **67**, 256–266.
47. W. S. Rasband, ImageJ 1.48, U. S. National Institutes of Health, Bethesda, Maryland, USA, http://imagej.nih.gov/ij/, 1997-2014
48. G. George and S. Anandhan, *J. Mater. Res.*, 2014, DOI: 10.1557/jmr.2014.233
49. F. Yener and O. Jirsak, *J. Nanomater.*, 2012, DOI: 10.1155/2012/839317
50. S. Anandhan, K. Ponprapakaran, T. Senthil and G. George, *Int. J. Plast. Technol.*, 2012, **16**, 101–116.
51. S. Tripatanasuwan and D. H. Reneker, *Polymer*, 2009, **50**, 1835–1837.
52. A. K. Zak, W. H. A. Majid, M. E. Abrishami and R. Yousefi, *Solid State Sci.*, 2011, **13**, 251–256.
53. T. Senthil and S. Anandhan, J. Colloid Interface Sci., 2014, 432, 285–296.

54. X. Zhang, W. Shi, J. Zhu, W. Zhao, J. Ma, S. Mhaisalkar, T. L. Maria, Y. Yang, H. Zhang, H. H. Hng and Q. Yan, *Nano Res.*, 2010, **3**, 643–652.
55. A. P. Grosvenor, M. C. Biesinger, R. S. C. Smart and N. S. McIntyre, *Surf. Sci.*, 2006, **600**, 1771–1779.
56. M. C. Biesinger, B. P. Payne, L. W. M. Lau, A. Gerson and R. S. C. Smart, *Surf. Interface Anal.*, 2009, **41**, 324–332.
57. N. Mironova-Ulmane, A. Kuzmin, I. Steins, J. Grabis, I. Sildos and M. Pärs, *J. Phys.: Conf. Ser.*, 2007, **93**, 012039.
58. M. Cardona, in *Raman Scattering in Materials Science*, eds. D. W. H. Weber and P. R. Merlin, Springer-Verlag, Berlin, 2000, pp. 151–225.
59. M. I. Kaganov, *Electrons, Phonons, Magnons*, Imported Pubn,, Chicago, 1981.
60. M. Lenglet, J. M. Machefert, J. Arsene, P. Leterrible, J. M. Welter, M. Lecalvar and R. Fontaine, *Surf. Interface Anal.*, 1988, **12**, 436–437.
61. K. Boubaker, *Eur. Phys. J. Plus*, 2011, **126**, 1–4.
62. B. Choudhury, M. Dey and A. Choudhury, *Int. Nano. Lett*., 2013, **3**, 1–8.
63. W.-B. Zhang, N. Yu, W.-Y. Yu and B.-Y. Tang, *Eur. Phys. J. B*, 2008, **64**, 153–158.
64. R. H. Kodama, *J. Magn. Magn. Mater*., 1999, **200**, 359–372.
65. Y. Wang, J. Chen and X. Wu, *Mater. Lett*., 2001, **49**, 361–364.
66. G. Martinelli, M. C. Carotta, M. Ferroni, Y. Sadaoka and E. Traversa, *Sens. Actuators, B*, 1999, **55**, 99–110.
67. X. Chu, X. Liu, G. Wang and G. Meng, *Mater. Res. Bull.*, 1999, **34**, 1789–1795.
68. K. Wetchakun, T. Samerjai, N. Tamaekong, C. Liewhiran, C. Siriwong, V. Kruefu, A. Wisitsoraat, A. Tuantranont and S. Phanichphant, *Sens. Actuators, B*, 2011, **160**, 580–591.
69. A. Afzal, N. Cioffi, L. Sabbatini and L. Torsi, *Sens. Actuators, B*, 2012, **171–172**, 25–42.
70. K. Arshak and I. Gaidan, *Mater. Sci. Eng., B*, 2005, **118**, 44–49.
71. N. Kumazawa, M. R. Islam and M. Takeuchi, *J. Electroanal. Chem*., 1999, **472**, 137–141.